Materials Advances

Accepted Manuscript

This article can be cited before page numbers have been issued, to do this please use: H. Yaqoob, N. Arif, R. S. Z. Saleem, J. I. Khan, R. S. Ashraf, C. Nielsen and G. A. Chotana, *Mater. Adv.*, 2026, DOI: 10.1039/D6MA00215C.

ROYAL SOCIETY OF CHEMISTRY

rsc.li/materials-advances

CF_3-Pyridyl-Substituted Hetero- and Homocyclic Conjugated Molecules: From Non-Emissive to Highly Emissive through Core Engineering

Hasan Yaqoob,[ab] Nimra Arif,[a] Rahman Shah Zaib Saleem,[a] Jafar Iqbal Khan,[c] Raja Shahid Ashraf,[d] Christian B. Nielsen,[b] Ghayoor Abbas Chotana[a*]

[a]Department of Chemistry and Chemical Engineering, SBA School of Science and Engineering, Lahore University of Management Sciences (LUMS), Sector U, DHA Lahore Cantt. 54792, Pakistan.

[b]Department of Chemistry, School of Physical and Chemical Sciences, Queen Mary University of London, London E1 4NS, UK.

[c]Department of Physics, School of Natural Sciences, University of Hull, Hull HU6 7RX, UK.

[d]Department of Chemistry, Institute of Chemical Sciences, Government College University Lahore, Punjab 54000, Pakistan.

E-mail: ghayoor.abbas@lums.edu.pk

Abstract

Herein, we report the synthesis of six CF_3-pyridyl-substituted aromatics via Suzuki–Miyaura cross-coupling, incorporating electronically diverse heterocyclic (pyrazine, benzothiadiazole) and homocyclic (chrysene, anthracene, pyrene, perylene) cores to systematically probe structure–property relationships. UV-Vis absorption, steady-state and time-resolved photoluminescence, electrochemical measurements, and quantum chemical calculations demonstrate that the homocyclic derivatives exhibit long fluorescence lifetimes (τ), high photoluminescence quantum yields (ϕ_{PL}), large dipole moment changes ($\Delta\mu$), optimally aligned frontier energy levels, and backbone-delocalized charge redistribution. Among these, anthracene-based compound (H-An) shows longest τ and highest ϕ_{PL} with strongly suppressed non-radiative decay, pyrene derivative (H-Py) displays the largest $\Delta\mu$, while the perylene analogue (H-Per) demonstrate red-shifted absorption, computed high light-harvesting efficiency, minimal exciton binding energy, and the lowest hole and electron reorganization energies, highlighting their potential as bright emitter or absorber for optoelectronic applications. In contrast, the heterocyclic compounds (H-Pz and H-BTD) are weakly emissive or nearly non-emissive, indicative of dominant non-radiative relaxation pathways. Density functional and time-dependent DFT calculations reproduce the experimental trends, underscoring that strategic core engineering within the CF_3-pyridyl framework is an effective approach for tuning optical, charge transport, and emissive properties in organic optoelectronic materials.

View Article Online
DOI: 10.1039/D6MA00215C

Introduction:

Strategic molecular design of π-conjugated molecules is central to advancing organic optoelectronic devices such as organic solar cells (OSCs), organic field effect transistors (OFETs), perovskite solar cells (PSCs), sensors, and organic light emitting diodes (OLEDs).[1, 2] Careful selection of central π-cores, terminal groups, and attached substituents allows precise tuning of frontier molecular orbitals (FMOs), molecular packing, charge transport, and photophysical properties.[3, 4] To achieve state-of-the-art organic functional materials, researchers have explored a variety of π-cores, including electron deficient heterocycles such as pyrazine[5] and benzothiadiazole[6] for their strong acceptor nature, and rigid homocycles such as chrysene,[7] anthracene,[8] pyrene,[9] and perylene[10] for their extended conjugation and excellent photo and thermal stability, embedding them with unique terminal groups such as pyridine,[11] quinoline,[12] and triarylamine.[13, 14] For example, in 2020, Marder's group investigated nine regioisomeric dipyridyl-pyrene derivatives and demonstrated the strong dependence of their photophysical properties on molecular design.[15] Similarly, Kido's group reported a terpyridine-modified chrysene derivative as an efficient electron transport layer (ETL) in ultra stable phosphorescent OLEDs, attributing its performance to planarity induced by the terpyridine moieties.[16] In 2023, Ren's group theoretically investigated the charge transport properties of 2,6-dipyridyl anthracene isomers and revealed superior charge transport for *meta* isomer compared to excellent 2,6-diphenyl anthracene molecule, mainly due to favourable intermolecular interactions **(Figure 1).**[17]

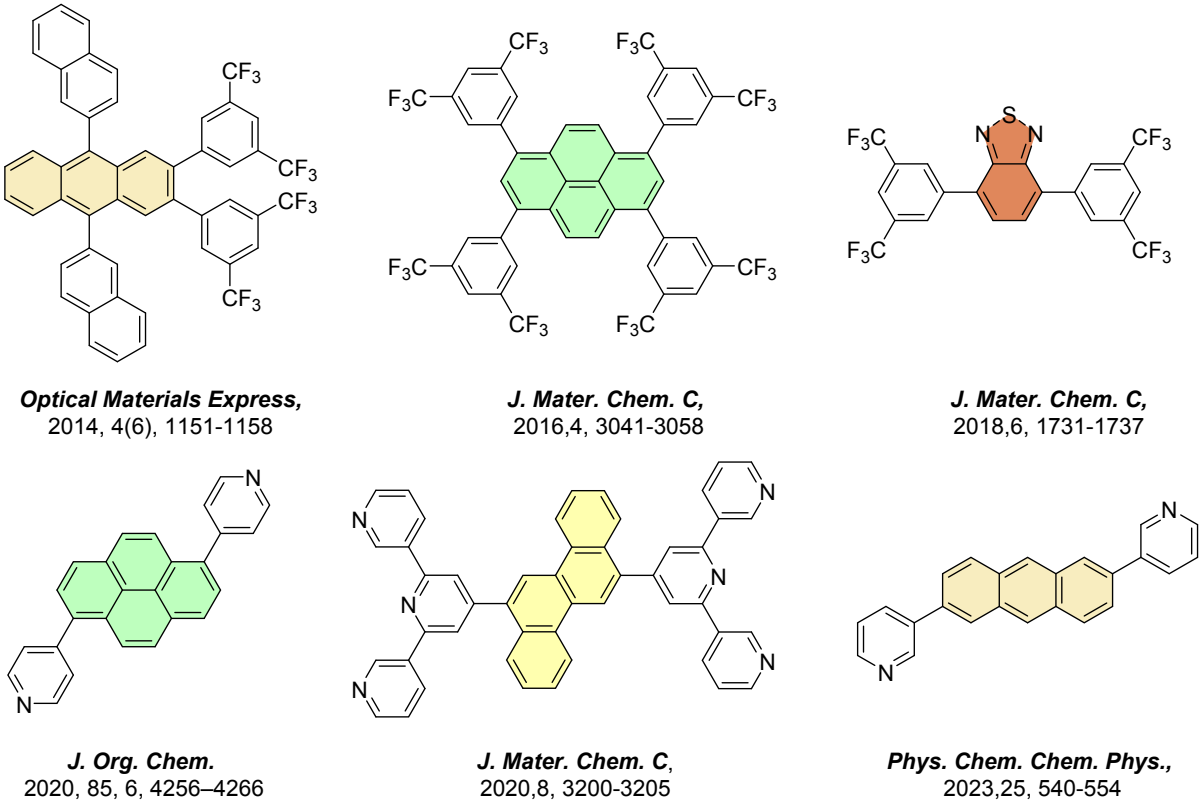

Figure 1. Selected examples of trifluoromethylated and pyridyl-substituted conjugated molecules reported in literature

View Article Online
DOI: 10.1039/D6MA00215C

Despite such progress, fluorination remains one of the most powerful strategies for achieving the desired optoelectronic properties.[18] Trifluoromethylated (-CF_3) compounds have been extensively used in fields ranging from pharmaceuticals to optoelectronic materials owing to their strong electron withdrawing effect and high electronegativity (3.5 on the Pauling scale).[19] Such remarkable features enable -CF_3 group to lower FMOs energy, improve optical properties, and facilitate non-covalent interactions(NCI) such as C–F...H, C–F...S, and C–F...π, ultimately influencing molecular packing, planarity, stability, and device performance.[20, 21] To exploit these advantages, researchers have widely incorporated -CF_3 substituents into π-conjugated scaffolds. For instance, Kaafarani's group synthesized nine 1,3,6,8-tetraarylpyrene derivatives, with selected candidates tested for OLEDs, and found the 3,5-bis-CF_3-substituted compound exhibited the highest absolute quantum yield (ϕ_{PL} = 0.918) in the crystalline state due to enhanced intermolecular interactions facilitated by CF_3 groups.[22] Similarly, Kim's group synthesized anthracene-based molecule featuring naphthalene units at the 9,10-positions and 3,5-bis(trifluoromethyl)phenyl units at the 2,3-positions; this compound demonstrated high thermal stability (5% weight loss at ~398 °C), stabilized FMOs, and high quantum efficiency resulting from CF_3-induced molecular twisting compared to CF_3-substituted analogues.[23] Additionally, Soulé's group reported Pd-catalyzed C–H bond arylation of 2,1,3-benzothia/selenadiazole derivatives, observed that among 4,7-diaryl-2,1,3-benzothiadiazoles, 3,5-bis(trifluoromethyl)phenyl substituted analogue displayed the highest quantum yield (ϕ_{PL} = 0.89) in thin films, depicted significantly better properties than non-fluorinated derivatives **(Figure 1)**.[24]

Although numerous reports describe -CF_3 group substituted or pyridyl-substituted π-conjugated systems, CF_3-substituted pyridyl bearing small π conjugated molecules remain underexplored. To the best of our knowledge, no systematic study has examined how incorporating CF_3-pyridyl terminal groups across electronically diverse π-cores ranging from electron-deficient heterocycles to electron-rich polyaromatics influences their electronic and photophysical behaviour. In our previous work, we reported the Ir-catalyzed C–H borylation of 2,6 bis(trifluoromethyl)pyridine in 2017,[25] which we later extended in 2022 to access 26 new CF_3-pyridyl boronic esters.[26] Building on this foundation and addressing this literature gap, we sought to investigate the structure–property relationships of CF_3-pyridyl-substituted π-conjugated molecules and to understand the role of core engineering in modulating their photophysical, electrochemical, charge transport and emissive properties.

In this context, we report the design and synthesis of six new 2,6-bis(trifluoromethyl)pyridyl-substituted π-conjugated molecules incorporating pyrazine, benzothiadiazole, chrysene, anthracene, pyrene, and perylene as central cores. These cores were selected for their contrasting electronic nature (electron-deficient vs electron-rich) and structural diversity (heteroaromatics vs (homo)polyaromatics), enabling a comparative investigation of their structure–property relationships. This study involves the photophysical, cyclic voltametric, and computational studies of all target compounds.

Methodology

The synthesis of all the target compound was carried out in the two steps as outlined in **Scheme 1.** Firstly, we carried out the Ir-catalyzed C-H activation of 2,6-bis(trifluoromethyl)pyridine to

View Article Online
DOI: 10.1039/D6MA00215C

access compound **A** by a protocol reported by Chotana's group.[25] Subsequently, compound **A** was subjected to Suzuki-Miyaura cross-coupling reaction with six dibromo-substituted π-aromatic cores to afford the target compounds (H-Y). All the target compounds were purified by column chromatography and obtained in good to excellent yields (61–92%). Finally, all compounds were characterized by FT-IR, GC–MS, and NMR spectroscopy **(Experimental Section and Figures S15-37)**.

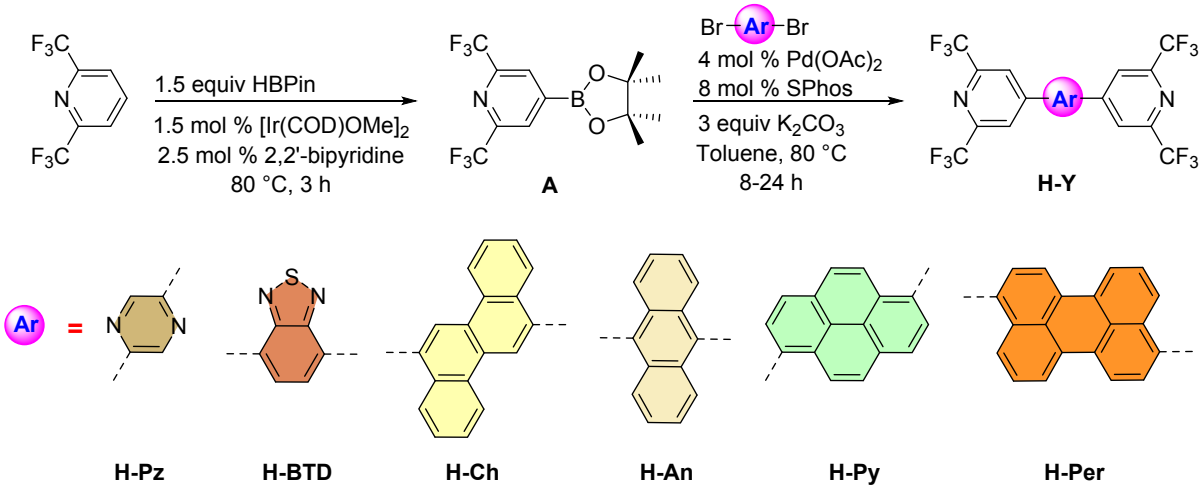

Scheme 1. Synthesis of all the target compounds reported in this study

Photophysical Properties

The comprehensive photophysical studies were carried out in solutions by using ten different solvents of varying polarity including nonpolar, polar aprotic, and polar protic with distinct dielectric constants and refractive indices. The absorption and emission spectra are given in **Figures 2 and S1-S2**, and the corresponding data is outlined in **Table 1 and S1**. In **Figure 2A**, all compounds display two main absorption bands. The high-energy band in the 248–281 nm region is assigned to localized π→π* transitions mainly associated with the CF_3-pyridyl terminal unit, while the broad low-energy band in the 309–461 nm region is attributed to mixed π→π* / ICT transitions involving the central core and the terminal pyridyl acceptor. The CF_3-pyridyl unit acts as a strong electron-withdrawing acceptor due to the combined -I effect of the CF_3 group and the electron-deficient pyridyl ring.[27] This leads to stabilization of the LUMO and provides the driving force for charge transfer from the central core toward the terminal units. This interpretation is consistent with related pyridyl based conjugated systems reported in the literature, where the higher-energy band corresponds to localized excitation and the lower-energy band charge transfer character.[27-29] TD-DFT results **(Tables S11–S22)** further support this, showing that the low-energy transition is dominated by HOMO→LUMO excitation with strong charge redistribution from the core toward the CF_3-pyridyl terminal rings. Conversely, higher-energy transitions involve multiple contributions from deeper occupied orbitals and higher unoccupied orbitals, confirming their localized π→π* character.

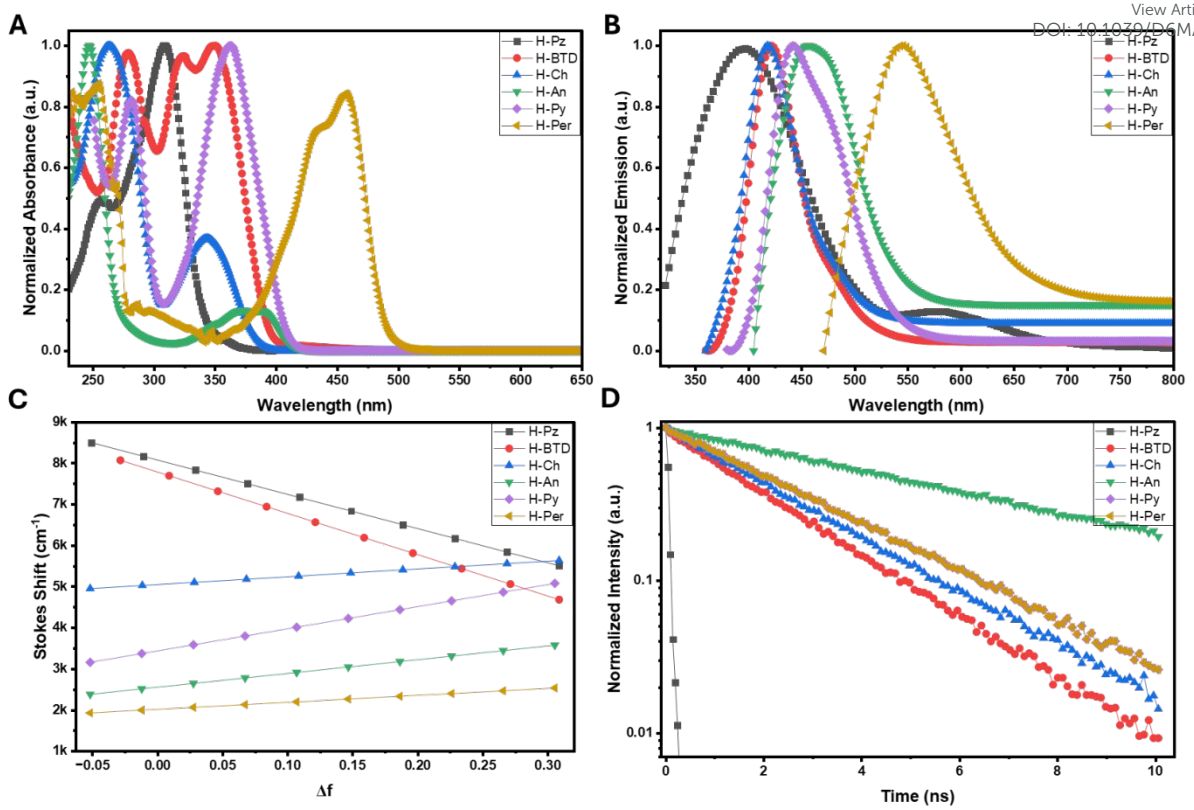

Figure 2. Photophysical Properties of all compounds **A.** UV-vis absorption spectra recorded in in $CHCl_3$ solution (conc. = 10^{-4} – 10^{-5} M) **B.** Emission spectra recorded in $CHCl_3$ solution conc. = 10^{-4} – 10^{-5} M) and excitation wavelengths in window of 20 nm lower and higher with respect to λ_{max} **C.** Fitted slopes comparison calculated from Lippert-Mataga analysis **D.** Normalized fluorescence lifetime decay plots recorded in $CHCl_3$ (Excitation wavelengths for H-Pz (374 nm), H-BTD (550 nm), H-Ch (566 nm), H-An (545 nm), H-Py (472 nm), H-Per (650 nm) and bandwidth (10 nm).

Overall, the absorption trend follows H-Per > H-An > H-Py > H-BTD > H-Ch > H-Pz. This trend is quantitatively supported by the HOMO-LUMO energy gaps obtained from electrochemical and computational analyses. The band gaps decrease systematically from H-Pz (4.01 eV) and H-BTD (3.53 eV) to H-Per (2.69 eV), indicating that extended π-conjugation in homocyclic cores effectively narrows the energy gap and facilitates lower-energy electronic transitions. A similar trend is observed in the computed energy gaps, further validating the experimental observations. Additionally, frontier molecular orbital distributions show that in homocyclic derivatives the HOMO is largely delocalized over the central aromatic core, while the LUMO extends toward the CF_3-pyridyl terminals, enabling more efficient intramolecular charge transfer. In contrast, heterocyclic systems exhibit relatively localized orbital distributions, which limits effective conjugation and results in higher-energy absorption bands.

On the other hand, the emission spectra **(Figure 2B)** show broad fluorescence bands in the 396–544 nm range, and the emission maxima follow the same trend, H-Per > H-An > H-Py > H-Ch ≈ H-BTD > H-Pz.

Table 1. Optical data for all compounds recorded in $CHCl_3$ where λ_{abs} = absorbance wavelength maxima, λ_{em} = emission wavelength maxima, $E_{0\text{-}0}$ = optical band gap (eV) =1240/(λ_{max}(nm), Stokes shift = $\Delta\nu$ (cm^{-1}), dipole moment change = $\Delta\mu$ (D), photoluminescence quantum yield = ϕ_{PL} and radiative and non-radiative constants = k_r, k_{nr}.

View Article Online
DOI: 10.1039/D6MA00215C

Compd	λ_{abs} (nm)	λ_{em} (nm)	E_{0-0} (eV)	$\Delta\nu$ (cm^{-1})	$\Delta\mu$ (D)	ϕ_{PL} (%)	τ (ns)	K_r 10^8 (s^{-1})	K_{nr} 10^8 (s^{-1})
H-Pz	256, 309	396	4.01	7109.9	-	-	0.060	-	-
H-BTD	279, 351	422	3.53	4793.4	-	7.6	2.088	0.37	4.42
H-Ch	264, 344	419	3.60	5203.4	10.30	72.3	2.378	3.04	1.16
H-An	248, 394	457	3.15	3498.9	10.88	94.6	6.212	1.52	0.09
H-Py	281, 368	442	3.37	4549.5	18.11	90.4	2.839	3.18	0.34
H-Per	256, 461	544	2.69	3309.6	11.87	86.9	2.839	3.06	0.46

To comprehend the solvents effect on the photophysical properties of the designed molecules, we carried out the Lippert-Mataga analysis.[30] This model treats the solute as a point dipole in a spherical cavity within a dielectric continuum and does not account for specific solute–solvent interactions such as hydrogen bonding, π–π stacking, aggregation, or charge transfer complex formation.[31-33] The absorption spectra show only minor changes with solvent polarity, indicating that the ground state is only weakly perturbed by the medium. This observation is consistent with the very small ground-state dipole moments (μ_g) predicted by DFT (0.0001–0.7786 D, **Table S4**). These low values are not computational artifacts but arise from the near-symmetric molecular architectures, where the individual dipole vectors of the CF_3-pyridyl units cancel each other. To verify this, we optimized homocyclic derivatives against four hybrid DFT functionals (B3LYP, CAM-B3LYP, MPW1PW91, and WB97XD, **Table S3**). All DFT functionals gave consistently low μ_g values, confirming that the small dipoles (μ_g) are intrinsic to their molecular symmetry.

In contrast, the emission spectra show pronounced solvatochromic shifts. For the homocyclic compounds, Stokes shift versus orientation polarizability (Δf) gives well-defined linear correlations with positive slopes, supporting a normal Lippert–Mataga response. The heterocyclic compounds H-Pz and H-BTD deviate from this behaviour and give negative slopes, indicating that the simple continuum model is not adequate for these compounds (**Figures 2C and S3)**. These deviations likely arise from specific solute–solvent interactions and excited-state stabilization, especially through heteroatom-solvent interactions, which are not captured by the Lippert–Mataga model. To further examine these effects, we carried out multi-parameter Kamlet–Taft analysis, which accounts for solvent polarity (π*), hydrogen-bond donor ability (α), and hydrogen-bond acceptor ability (β) **(Figure S5)**.[34] For H-Pz, the strong dependence on solvent basicity (β) suggests specific hydrogen-bonding interactions between solvent molecules and the pyridine/pyrazine nitrogen atoms, which stabilize the excited state. For H-BTD, the poor regression fit indicates a more complex solvent response, likely influenced by the sulfur-containing core. Thus, in our hands, the Lippert–Mataga model works well for the homocyclic cores but shows limitations for the heterocyclic derivatives due to dominant specific solute–solvent interactions.

For the homocyclic derivatives, excited-state dipole moments (μ_e) were calculated using ground-state dipole moments (μ_g) and Onsager radii (a) obtained from DFT-optimized geometries **(Table S4)**, following the methodology reported by Wee's group.[35] The calculated $\Delta\mu$ values follow the order H-Py > H-Per > H-An > H-Ch, consistent with the relative steepness of the Lippert–Mataga slopes. The large μ_e (10.30–18.11 D) clearly indicate substantial charge redistribution upon photoexcitation, confirming efficient charge transfer across these

View Article Online
DOI: 10.1039/D6MA00215C

molecules.[36] This is further supported by the natural population analysis (NPA) **(Figure S38)**, where the charge distribution is clearly shifted toward CF_3-pyridyl units. The homocyclic systems show larger core-to-terminal charge separation than the heterocyclic analogues, with the NPA values decreasing in the order H-Per (+0.08846) > H-Py (+0.08237) > H-Ch (+0.07578) > H-An (+0.05829) > H-Pz (+0.03188) > H-BTD (+0.02474). This clearly shows that the homocyclic derivatives possess stronger ICT character, while the heterocyclic compounds exhibit weaker charge redistribution.

Fluorescence lifetimes (τ) and photoluminescence quantum yields (ϕ_{PL}) were measured in chloroform, and the radiative (K_r) and non-radiative (K_{nr}) decay constants were calculated from the ϕ_{PL} and τ **(Table 1, Figure 2D, and Figures S4, S8-S12)**. All compounds exhibit predominantly single-exponential decay profiles, indicating the presence of a single emissive excited state. Compounds containing homocyclic aromatic cores show significantly higher ϕ_{PL} values (72.3–94.6%) and longer lifetimes (2.378–6.212 ns) compared to heterocyclic analogues. This behaviour can be attributed to the rigid, planar, and π-extended nature of the homocyclic frameworks, which suppress vibrational relaxation and favour radiative decay pathways.[15, 37] Correspondingly, these compounds exhibit relatively high K_r in the range of ~1-3 $\times$ 10^8 s^{-1}.

Interestingly, among all compounds, H-An exceptionally demonstrated highest ϕ_{PL} of 94.6 % with τ (6.212 ns) with lowest K_{nr}, because of its linear three acene rings geometry promotes efficient π-delocalization while minimizing non-radiative deactivation pathways such as internal conversion and intersystem crossing.[38] In contrast, H-BTD have shown the lowest ϕ_{PL} of 7.6 % mainly because of presence of heteroatoms like S in the central core. This quenching may be attributed to fast non-radiative decay, likely via enhanced intersystem crossing (sulfur-mediated SOC) and/or rapid relaxation to a non-emissive CT minimum, which is further supported by problematic Lippert-Mataga slopes and the divergence between TDDFT oscillator strength and observed emissive efficiency.[39, 40]

Electrochemical Properties

The electrochemical behaviour of the compounds was investigated by cyclic voltammetry (CV) and differential pulse voltammetry (DPV) in anhydrous DCM using 0.1 M Bu_4NPF_6 as the supporting electrolyte in a three-electrode setup, i.e., glassy carbon as the working electrode, Pt wire as the counter electrode, and Ag/AgCl as the reference electrode. Ferrocene was measured as an internal standard under identical conditions, and its oxidation potential was determined to be 0.26 V **(Figure S14a).** Oxidation potentials (E^o_{Oxi}) for all compounds were determined from the oxidation peak potentials obtained from Differential Pulse Voltammetry (DPV, **Figure 3**) and supported by Cyclic Voltammetry (CV, **Figure S13**) and all values are referenced directly to Fc/Fc^+.

In **Figure 3**, heterocyclic compounds H-Pz and H-BTD exhibit two well-defined reduction peaks (for H-Pz: -1.20 V and -1.60 V; for H-BTD: -1.09 V and -1.42 V) in the cathodic region, indicating sequential one-electron reduction processes from the neutral molecule to the radical anion and then to the dianion. This behaviour arises from the electron-deficient nature of the central cores (Pz and BTD), which stabilise the added electrons.[41-43] The frontier molecular orbital (FMOs) analysis **(Figure 5A)** shows that the LUMO and LUMO+1 are primarily

View Article Online
DOI: 10.1039/D6MA00215C

localized on the electron-deficient central core, supporting the stepwise electron uptake and stabilization of the reduced species. In contrast, the homocyclic analogues generally show a single reduction peak, indicating that further reduction is less favourable under the same conditions. This can be attributed to their extended central cores, which result in a different spatial distribution of the LUMO and LUMO+1 orbitals. Specifically, in these molecules, the LUMO is primarily localized on the central core, while the LUMO+1 is shifted towards the terminal CF_3-pyridyl rings with increased energy, thereby limiting additional electron accommodation.

Table 2. Electrochemical data: [a]calculated from oxidation peak potentials of differential pulse voltametric (DPV) traces, [b] computed DFT values

Compd	E^{o}_{Oxi} (V)	HOMO[a] (eV)	LUMO[a] (eV)	E_g[a] (eV)	HOMO[b] (eV)	LUMO[b] (eV)	E_g[b] (eV)
H-Pz	1.62	-6.29	-2.28	4.01	-7.74	-3.34	4.40
H-BTD	1.63	-6.30	-2.77	3.53	-7.21	-3.56	3.65
H-Ch	1.65	-6.32	-2.72	3.60	-6.24	-2.50	3.74
H-An	1.42	-6.09	-2.94	3.15	-6.0	-2.53	3.47
H-Py	1.44	-6.11	-2.74	3.37	-6.08	-2.66	3.42
H-Per	1.05	-5.72	-3.03	2.69	-5.67	-2.83	2.84

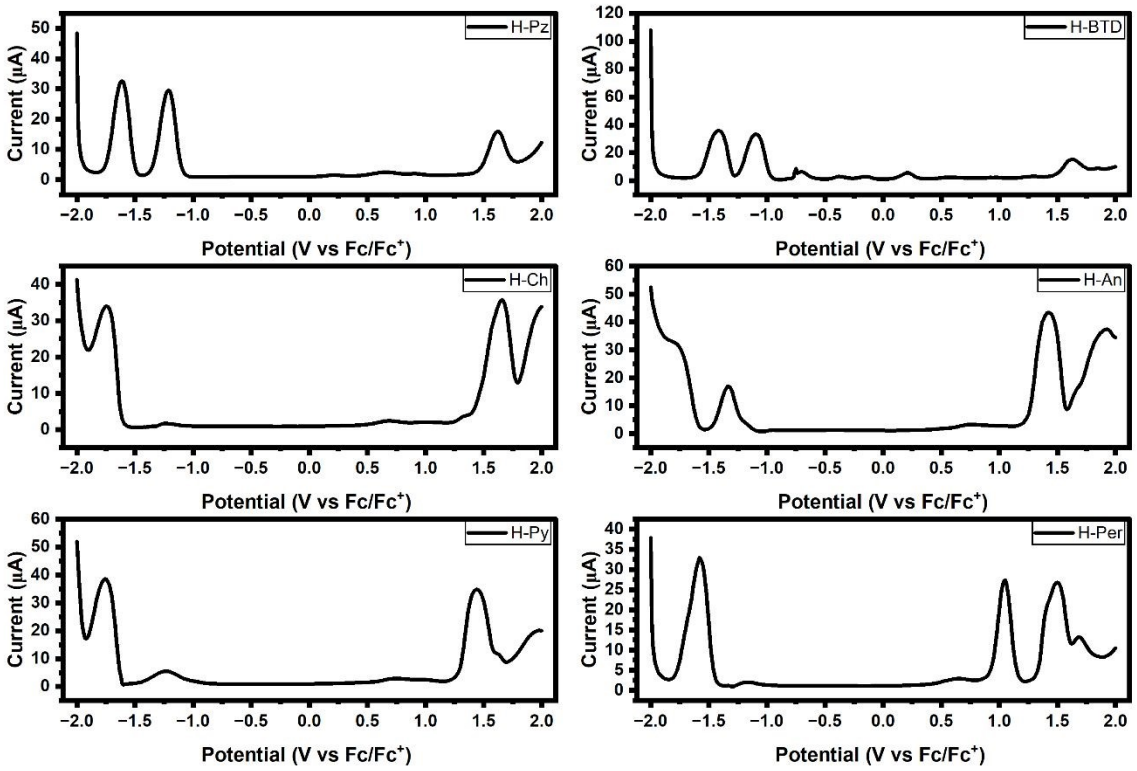

Figure 3. Differential pulse voltametric (DPV) traces for all compounds acquired in 0.1 M Bu_4NPF_6 as supporting electrolyte in anhydrous DCM solvent at 100 mV/s scan rate and potential window potential (-2 – 2 V)

View Article Online
DOI: 10.1039/D6MA00215C

Similarly, trends in the E^{o}_{Oxi} also vary across the series. The heterocyclic compounds (H-Pz and H-BTD) show single oxidation peaks at +1.62 V and +1.63 V, respectively. The relatively higher E^{o}_{Oxi} values of these compounds reflect the stabilization of the HOMO by the electron-deficient cores, making oxidation less favourable.[44] In contrast, among the homocyclic compounds, H-Per shows two distinct oxidation peaks (at +1.05 V and +1.49 V), indicating the two-step oxidation processes. This behavior is attributed to the extended π-conjugation of the perylene core, which enables effective delocalization of positive charge and stabilizes both oxidized states.[45] This is consistent with the HOMO and HOMO-1 distribution over the central core obtained from DFT calculations. Overall, E^{o}_{Oxi} values follow the order H-Per < H-An < H-Py < H-Ch, indicating that H-Per possesses the highest-lying HOMO, while H-Ch has the deepest HOMO among the homocyclic compounds. The deeper HOMO of H-Ch may be arisen from its specific 6,12-substitution pattern, which limits conjugation and reduces core electron density.

Overall, E_{HOMO} of the heterocyclic compounds (H-Pz, H-BTD) are lower than those of the homocyclic compounds, except for H-Ch. This is mainly due to the presence of heteroatoms (N and S) in the heterocyclic cores, which stabilize the molecules through their strong inductive effect. [46] The experimentally derived and computed HOMO-LUMO energy levels follow the same systematic trend and are in good agreement, confirming the reliability of the electronic structure analysis across the series.

Computational Studies

Optimized Geometry and Molecular Electrostatic Potential (MEP) Analyses

Density functional theory at B3LYP/6-31G(d,p) level was used to optimize all structures and to evaluate the ground-state geometries (**Figure 4A)**. In every compound the central aromatic core is essentially planar, whereas the CF_3-pyridyl terminals adopt out-of-plane orientations with distinct dihedral angles relative to the core.

The heterocyclic series displays the smallest dihedral angles, with H-Pz (15.0°) and H-BTD (34.5°), consistent with reduced rotational freedom arising from competing electron-withdrawing effects between the core and the terminals. By contrast, homocyclic cores show substantially larger twists in the order H-An > H-Ch > H-Per > H-Py, reflecting the greater electron density and steric crowding of extended aromatic systems. Importantly, H-An adopts the largest ground-state dihedral (82.5°), which indicates reduced ground-state conjugation with the terminals effectively decoupled.[47] Geometry relaxation on the S_1 surface drives partial planarization in H-An; the S_1 minimum is closer to planarity (dihedral angle 124.2°), corresponding to a decrease in distance to the nearest planar value by ~26.9° (**Figure S39)**. This excited-state planarization increases backbone conjugation, stabilizes S_1 and correlates with the observed long fluorescence lifetime (6.212 ns).[47] These observations underscore the central role of ground- and excited-state geometry in controlling intramolecular charge redistribution and PL efficiency.

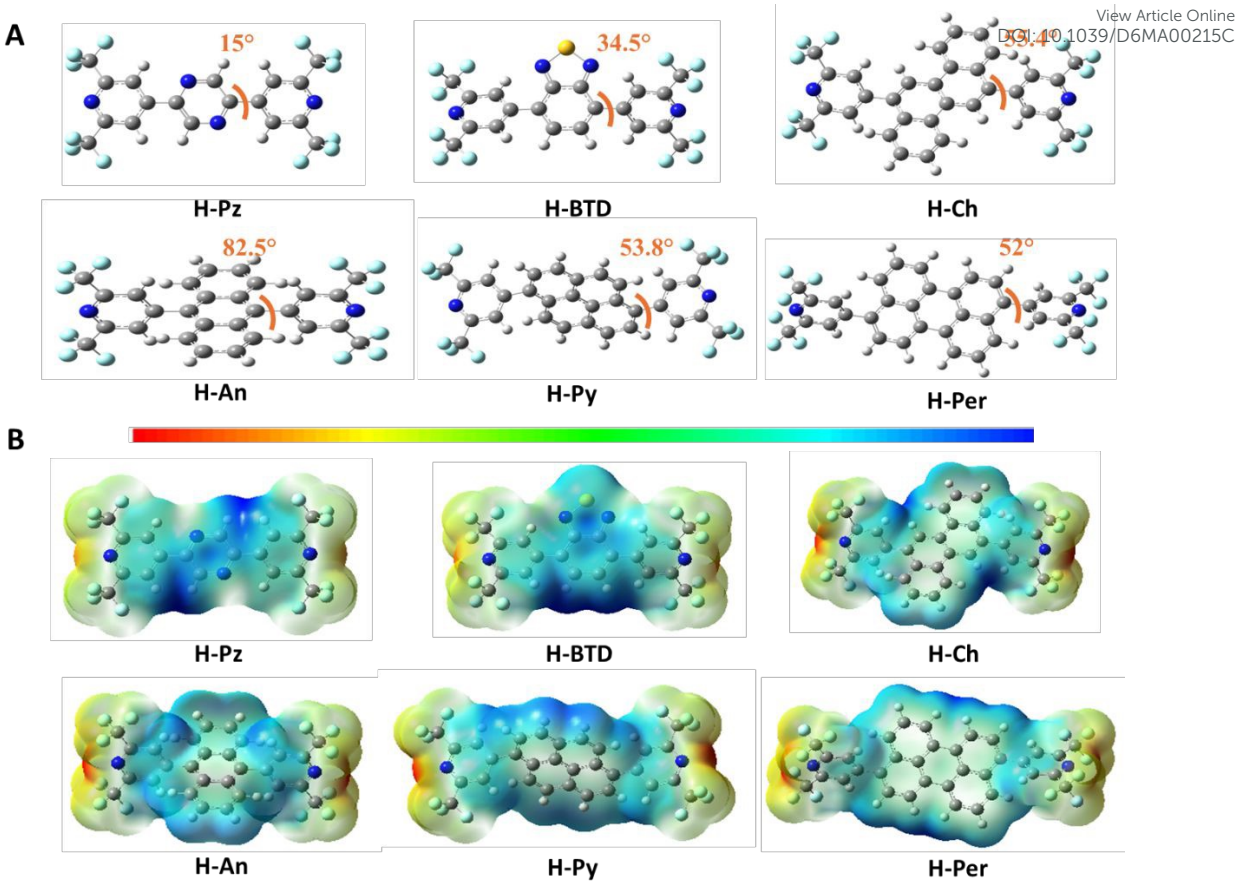

Figure 4. **A.** Optimized Geometry with dihedral angles **B.** Molecular Electrostatic Potential (MEP)

Molecular electrostatic potential maps provide a qualitative view of charge distribution and reactive sites.[48] In **Figure 4B,** the heterocyclic cores (Pz, BTD) exhibit positive potential regions on the ring nitrogens consistent with electron deficiency, whereas the CF_3-pyridyl terminals show negative potential on the pyridyl nitrogens consistent with acceptor character. Homocyclic cores display more uniformly negative potential over the aromatic backbone reflecting extended π electron density. These MEP plots support the interpretation that heterocycles act as strong acceptors while the large homocyclic cores behave as electron-rich backbones in the push-pull systems.

Frontier Molecular Orbitals (FMOs) and Density of States (DOS) Analyses

Frontier molecular orbitals (FMOs) analysis reveals the distinct distribution pattern of frontier orbitals in all molecules because of the electronically diverse central cores and this distribution aligned well with the DOS plots (**Figure 5 and Table 3)**.

View Article Online
DOI: 10.1039/D6MA00215C

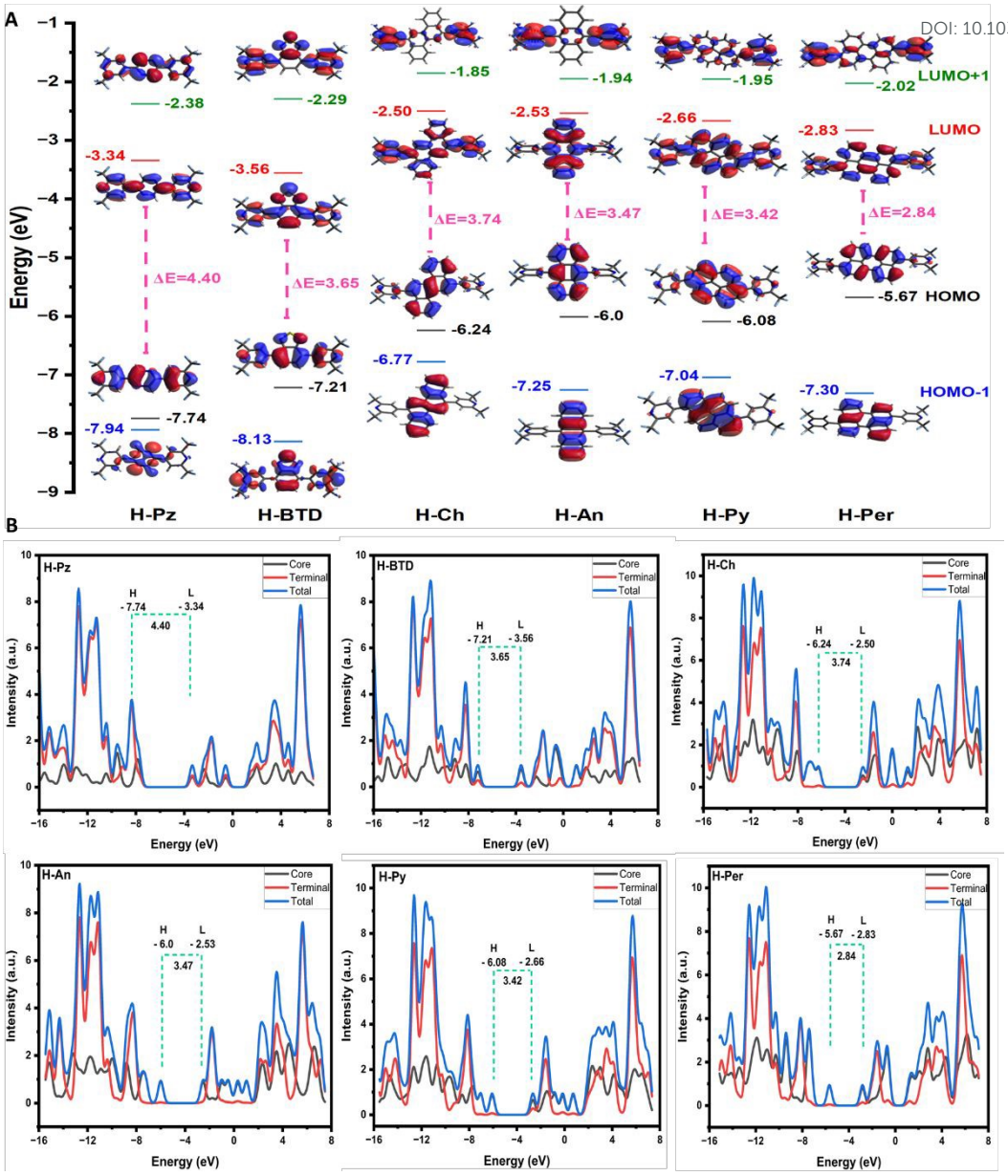

Figure 5. A. Frontier molecular orbital (FMOs) at their definite energy levels where E_g is the energy gap between HOMO and LUMO **B.** Density of states (DOS) plots for all synthesized compounds at B3LYP/6-31G(d,p) level of theory

For homocyclic A–D–A systems both HOMO and LUMO are dominated by core contributions (core contributions ~ 70–97%) that is the result of the intrinsic π-rich character of extended aromatic cores. Thus, the pronounced core weight of both HOMO and LUMO does not contradict a push-pull design but rather implies that charge redistribution on excitation is delocalized over the conjugated backbone instead of being concentrated at terminal groups.[49] Moreover, experimental Δμ values (10.30–18.11D) for these systems indicate substantial excited-state dipole change despite strong LUMO core character. In contrast, H-Pz shows a balanced HOMO/LUMO distribution (HOMO ~51% core, LUMO ~53% terminal) consistent with core-to-terminal separation and the heterocyclic acceptor character.

View Article Online
DOI: 10.1039/D6MA00215C

Table 3. Density of states (DOS) fragment orbital contribution

Compd	HOMO		LUMO	
	Core	Terminal	Core	Terminal
H-Pz	51	49	47	53
H-BTD	70	30	81	19
H-Ch	92	8	59	41
H-An	97	3	95	5
H-Py	93	7	70	30
H-Per	94	6	85	15

Furthermore, computed HOMO-LUMO gaps (2.84-4.40 eV) reproduce the experimentally calculated energy gaps that validates the accuracy of chosen B3LYP/6-31G(d,p) level of theory.

Time Dependant (TD) DFT Studies

Time-dependent TD-DFT calculations were performed at the B3LYP/6-31G(d,p) level in both the gas phase and with chloroform as an implicit solvent to validate the experimentally observed photophysical trends (**Figure 6** and **Table 4)**.

For all compounds, the lowest-energy singlet excitation ($S_0 \rightarrow S_1$) is majorly contributed by a HOMO→LUMO transition **(Tables S11–S22)**. The calculated absorption maxima showed close agreement with the experimental trends following the H-Per > H-An > H-Py > H-BTD > H-Ch > H-Pz. In all cases, implication of chloroform solvent leads to a bathochromic shift relative to the gas phase, reflecting stabilization of the excited states by the polar medium.[50] Similarly, oscillator strengths (*f*) and light-harvesting efficiencies (LHE) are systematically enhanced in chloroform compared to the gas phase, indicating more efficient light absorption under solvated conditions.[51]

Among the series, H-An exhibits the lowest *f*, which can be attributed to its relatively orthogonal ground-state geometry that reduces the transition dipole moment and limits effective orbital overlap between the ground and excited states, leading to a more localized excitation on the central anthracene core as evident in the CDD surface contours.[47, 52] In contrast, H-Pz shows comparatively large *f* and LHE despite being non-emissive, suggesting that strong optical absorption doesn't always results in radiative decay when non-radiative relaxation pathways dominate.[49] Overall, the TD-DFT results reveal the absorption and electronic trends across the series, while clearly distinguishing excitation probability from emission efficiency.

View Article Online
DOI: 10.1039/D6MA00215C

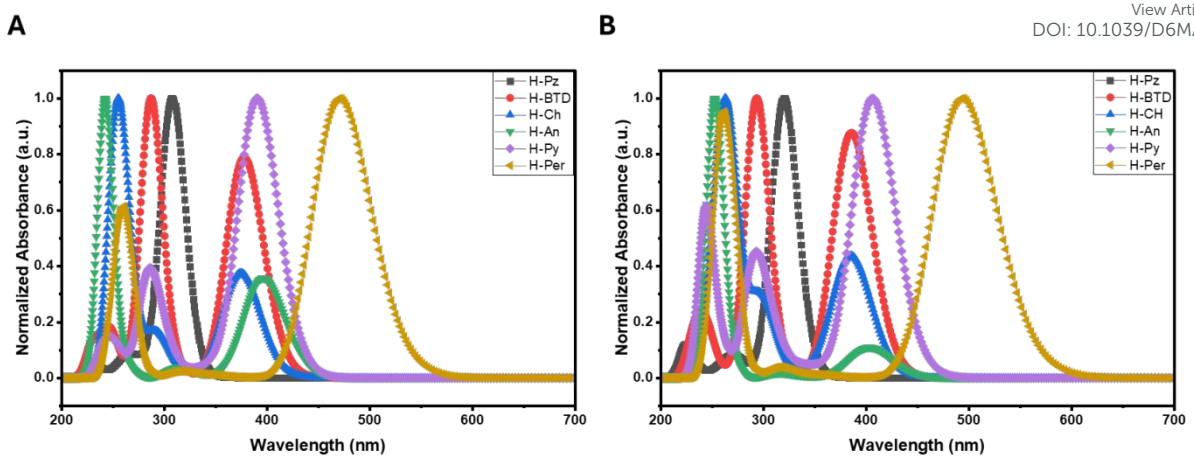

Figure 6. Computed UV-Vis profiles for all compounds **A.** Gaseous phase **B.** Chloroform medium

Table 4. Computed TD-DFT parameters at B3LYP/6-31G(d,p) for all compounds where E_x is Excitation energy, *f* is Oscillator strength, and LHE is Light harvesting efficiency.

	Gaseous					Chloroform				
Compd	**λ_{abs} (nm)**	**E_x (eV)**	***f* (au)**	**LHE**	**Major transition (%)**	**λ_{abs} (nm)**	**E_x (eV)**	***f* (au)**	**LHE**	**Major Transition (%)**
H-Pz	308 262	4.03 4.73	0.94 0.06	0.885	H→L (97) H→L+1 (70)	321 274	3.86 4.53	1.11 0.05	0.922	H→L (98) H-2→L (51)
H-BTD	378 286	3.28 4.33	0.38 0.35	0.580	H→L (98) H→L+1 (70)	387 303	3.20 4.10	0.49 0.18	0.678	H→L (99) H-1→L (88)
H-Ch	375 255	3.30 4.85	0.42 0.68	0.616	H→L (97) H-1→L+4 (61)	386 272	3.21 4.56	0.54 0.45	0.710	H→L (98) H-1→L+2 (86)
H-An	396 241	3.13 5.14	0.16 0.23	0.305	H→L (97) H-5→L (43)	403 252	3.08 4.92	0.20 1.57	0.370	H→L (96) H→L+5 (46)
H-Py	390 285	3.17 4.35	0.62 0.22	0.762	H→L (94) H→L+5 (44)	407 291	3.04 4.26	0.79 0.30	0.837	H→L (96) H→L+5 (58)
H-Per	471 263	2.63 4.70	0.73 0.26	0.814	H→L (99) H-2→L+7 (38)	493 268	2.51 4.63	0.89 0.34	0.871	H→L (99) H→L+7 (36)

Intramolecular Charge Transfer, Transition Density Matrices, Exciton Binding, and Reorganization Energies Analyses

Charge density difference maps visualize the spatial redistribution of electron density upon photoexcitation from ground to excited state.[53] The CDD Maps **(Figure 7A)** represents the distinct distribution patterns based on the molecular design. Generally, In the homocyclic A–D–A series the hole distribution is concentrated on the core (~92–97%) while the electron

View Article Online
DOI: 10.1039/D6MA00215C

distribution retains a large core character but with measurable terminal participation (terminal electron contribution ~5–41%). This pattern indicates backbone-delocalized ICT rather than a strictly localized Core→terminal accumulation.

Transition density matrices provide atom-pair resolution. In all compounds the Core-Core block dominates the TDM, indicating that the core atoms contribute the largest atom-pair transition density **(Figure 7B)**. The magnitude of the core-terminal off-diagonal blocks discriminate CT from LE behaviour. H-Pz shows pronounced off-diagonal intensity and enhanced terminal-terminal signal, consistent with clear core→terminal CT. H-Ch and H-Py show intermediate off-diagonals and thus represent delocalized ICT. H-An and H-Per display dominant diagonal core-core intensity and weak off-diagonals, consistent with localized or backbone-delocalized excitations.

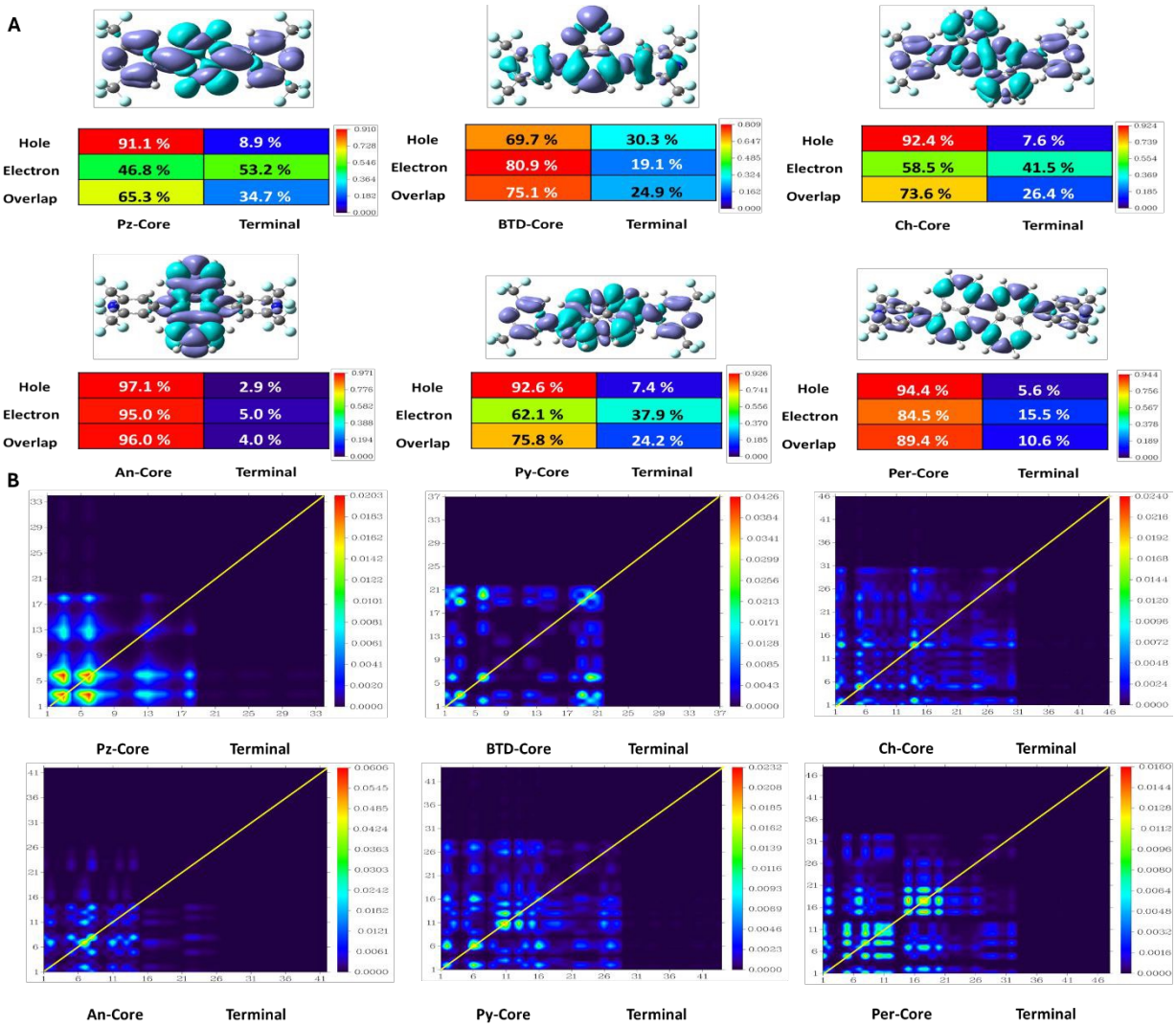

Figure 7. A. Charge density difference (CDD) surface contours where blue colour represent electrons and cyan shows holes, and corresponding hole/electron heat maps with % delocalization and overlap between two fragments (core and terminal) **B.** Transition Density Matrices heat maps at B3LYP/6-31G(d,p) level of theory

View Article Online
DOI: 10.1039/D6MA00215C

Additionally, total charge transfer and its %age contribution are computed from the excited-state density using fragment population analysis. These values give an idea about how much the electron density is transferred between the two fragments upon excitation.[54] For the homocyclic derivatives, the computed fragment charge transfer is comparatively lower (7.66–42.77%), while the locally excited (LE) contribution is dominant (57.23–92.34%). This lower q_{CT} does not imply the absence of charge transfer; rather, it shows the limitation of fragment-based metrics, which quantify population transfer between predefined fragments.[55] In these systems, excitation is largely delocalized over the extended aromatic backbone, resulting in significant charge redistribution without strong accumulation on the terminal units. This interpretation is consistent with the large experimentally observed Δμ values, which capture global dipole changes over long intramolecular distances rather than localized fragment-to-fragment transfer.[36]

Table 5. Charge Transfer parameters where total transferred charge (q_{CT}), charge transfer (CT) excitation, localized excitation (LE), exciton binding energy (E_b) and reorganization energy for holes and electrons respectively (λ_h, λ_e) for all compounds

Compd	q_{CT} (e^-)	CT (%)	LE (%)	E_b	λ_h	λ_e
H-Pz	0.442	52.611	47.389	0.306	0.340	0.449
H-BTD	0.112	37.838	62.162	0.372	0.314	0.547
H-Ch	0.338	42.765	57.235	0.432	0.192	0.546
H-An	0.020	7.659	92.341	0.344	0.193	0.688
H-Py	0.305	39.717	60.283	0.246	0.19	0.488
H-Per	0.099	19.324	80.676	0.212	0.167	0.396

Overall, H-An exhibits the most pronounced LE character (92.34%), in agreement with its molecular geometry and electronic structure. The nearly linear anthracene core promotes excitation localization on the central backbone, leading to weak core-terminal and strong core-core diagonal coupling as evident in TDM, along with minimal terminal contribution in the CDD maps, and the lowest *f* computed TD-DFT calculations.[47] Together, these observations confirm that photoexcitation in H-An is predominantly localized on the anthracene core, with limited charge separation, distinguishing it from the more delocalized ICT behaviour observed in H-Ch and H-Py. In contrast, H-Pz is the most canonical fragment CT molecule in the series. Next, Exciton binding energy (E_b) and reorganization energy for hole and electron (λ_h, λ_e) are computed to determine the propensity for exciton dissociation and the intrinsic carrier mobility **(Figure 8 and Table 5)**.[56] Among all, H-Per has the lowest E_b and thus the most favourable tendency for the exciton dissociation, whereas H-Ch and H-BTD have the largest E_b values and are least likely to generate free charges without an appropriate heterojunction.

Generally, Hole reorganization energies are generally small for extended cores (H-An, H-Py H-Per) and larger for heterocycles such as H-Pz ($\lambda_h \approx 0.341$ eV). Electron reorganization energies are higher across the series ($\lambda_e \approx 0.396$–0.688 eV) and therefore limit electron mobility relative to holes.

View Article Online
DOI: 10.1039/D6MA00215C

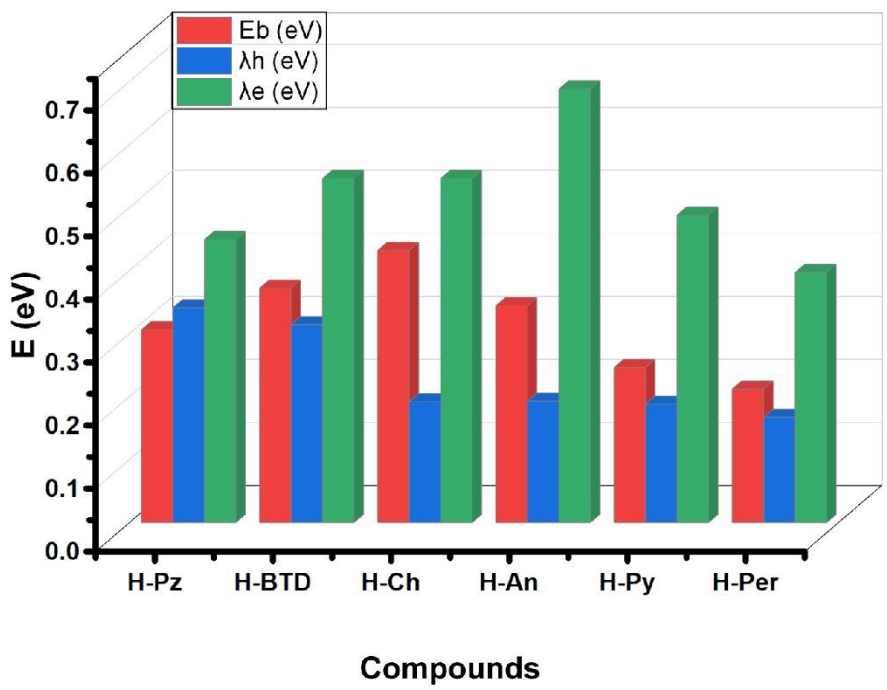

Figure 8. Exciton Binding and Reorganization energies of all compounds

Conclusively, the above results indicate that a high fragment CT contribution alone, as observed for H-Pz, does not guarantee efficient optoelectronic performance; rather, additional parameters such as E_b, λ_h and λ_e must be considered. Overall, homocyclic core containing compounds exhibit backbone-delocalized excitations with balanced charge redistribution and more favourable charge transport characteristics, whereas heterocyclic core-based molecules tend to show localized excitations and therefore require further molecular engineering to achieve comparable performance.

Among the series, H-An displays a long τ, highest ϕ_{PL}, lowest K_r, and dominant core-localized excitation (LE), highlighting its potential as an efficient emitter. In contrast, H-Py shows the largest $\Delta\mu$ upon excitation, while H-Per combines red-shifted absorption, lowest E_b, high LHE, and the lowest λ_h and λ_e, underscoring its suitability for charge transport applications.

Conclusions

The control of photophysical properties such as absorption, emission, fluorescence lifetime, absolute photoluminescence quantum yield, optimized frontier molecular orbital energies, along with efficient charge transport characteristics, is crucial for the design of promising optoelectronic materials. In this work, we synthesized, characterized, and systemically studied the photophysical, electrochemical and computational properties of six CF_3-pyridyl substituted conjugated materials based on electronically diverse heterocyclic and homocyclic aromatic cores. Interestingly, H-An exhibits a long fluorescence lifetime (τ = 6.212 ns), high ϕ_{PL} (94.6 %), and lowest non-radiative decay rate, which is attributed to its linear acene-type structure. H-Py demonstrates the largest dipole-moment change, indicative of a backbone-delocalized intramolecular charge transfer character, while H-Per shows red-shifted absorption, greenish fluorescence, and favourable charge transport properties. In contrast, heterocyclic cores display

View Article Online
DOI: 10.1039/D6MA00215C

low ϕ_{PL} and short lifetimes (τ = 0.06–2.38 ns), suggesting that excited-state relaxation is dominated by vibrational non-radiative pathways.

Through molecular design, absorption (309–461 nm), emission (396–544 nm), emission colour (ranging from non-emissive to bluish and greenish), $\Delta\mu$ (10.3–18.11 D), ϕ_{PL} (7.6–94.6 %), frontier orbital energy levels (HOMO -5.72 to -6.32 eV; LUMO -2.28 to -3.03 eV), and key computed parameters including dihedral angles (15–82.5°), light-harvesting efficiency (0.37–0.92), exciton binding energy (0.212–0.306 eV), reorganization energies (λ_h = 0.167–0.340 eV; λ_e = 0.396–0.688 eV), and fragment-based charge transfer (0.020–0.442 e^-) were effectively tuned. Conclusively, these results emphasize that strategic core engineering is an effective tool for modulating the photophysical, electrochemical, and charge transport properties of organic optoelectronic materials.

Experimental Section

Materials and Methods

All chemicals were purchased from commercial suppliers and used as received without further purification. Solvents employed for column chromatography were obtained commercially and distilled prior to use.

Absorbance and steady-state emission measurements were performed on solutions with concentrations in the range 10^{-4} – 10^{-5} M A Shimadzu1800 spectrophotometer was used for UV-Vis measurements over the wavelength range 200–800 nm, while steady-state fluorescence spectra were recorded on an Agilent Cary Eclipse spectrofluorometer. Fluorescence lifetimes were measured on an Edinburgh Instruments FLS1000, and absolute photoluminescence quantum yields (ϕ_{PL}) were determined using the integrating-sphere accessory of the same instrument. For the PLQY (ϕ_{PL}) measurements, the solutions were freshly prepared, and their absorbance was strictly controlled below 0.1 (**Figure S6)** to avoid any solute-solvent interactions, formation of aggregates, π-π stacking, and self-reabsorption of the emitted photons. For H-Pz compound, we couldn't measure the ϕ_{PL} because of its non-emissive nature as well as unavailability of the filters for the lowest absorbed materials (~ 310 nm) at our facility. NMR (^{1}H, ^{13}C and ^{19}F) spectra were recorded on Bruker spectrometers operating at 600 and 400 MHz. $CDCl_3$ was used as the primary solvent; for samples with limited solubility, DMSO-d_6 and acetone-d_6 were also used added. Molecular ion peaks were obtained by GC Trace-1300 coupled with MS and autosampler AI-1310, Thermo Scientific, while high-resolution mass spectra for H-Py and H-Per were acquired on a Waters Synapt G2-Si High-Definition Mass spectrometer **(Figures S13-19)**. IR spectra were recorded on a Bruker ATR-FTIR spectrometer **(Figure S12)**. Melting points were determined using a standard capillary melting-point apparatus (SMP30).

The experimental dipole moment change was calculated by Lippert-Mataga relationship as shown in eq (i)

$$\Delta\nu = \frac{2(\mu_e - \mu_g)^2}{4\pi\varepsilon_0 hca^3}\Delta f + constant \qquad \text{(i)}$$

Where Δν represents the Stokes shift (cm^{-1}), μ_g and μ_e are the ground and excited state dipole moments, respectively (D), h is Planck's constant, c is the speed of light, a is the Onsager cavity radius (Å), and Δf is the orientation polarizability parameter defined by eq (ii):

$$\Delta f = \frac{\varepsilon - 1}{2\varepsilon + 1} - \frac{n^2 - 1}{2n^2 + 1} \quad \text{(ii)}$$

The dielectric constants along with refractive indices for the solvents used in this study are toluene (2.38, 1.496), hexane (1.88, 1.372), petroleum ether (1.84, 1.357), cyclohexane (2.02, 1.426), chlorobenzene (5.62, 1.525), DCM (8.93, 1.424), THF (7.58, 1.407), acetonitrile (35.9, 1.344), MeOH (32.6, 1.328) and DMF (36.7, 1.4305) respectively. The radiative and non-radiative constants were calculated by the following eq (iii and iv)

$$K_r = {}^{\tau}/_{\phi} \quad \text{(iii)}$$

$$K_{nr} = 1 - {}^{\phi}/_{\tau} \quad \text{(iv)}$$

Cyclic voltammetry (CV) and Differential pulse voltammetry (DPV) were performed on PalmSens 3 e-chem instrument using a three-electrode setup i.e. glassy carbon working electrode, platinum wire counter electrode, Ag/AgCl reference electrode, while ferrocene/ferrocenium ion (Fc/Fc^+) as internal standard. Measurements were carried out in anhydrous DCM with 0.1 M tetrabutylammonium hexafluorophosphate (Bu_4NPF_6) as the supporting electrolyte and the analyte (3mg/5 mL). E_{HOMO} of all compounds was estimated from the oxidation peak potentials of DPV traces by eq (v) while and E_{LUMO} by difference of E_{HOMO} and the optical band gap using the eq (vi). In our hands, E^{o}_{Oxi} of ferrocene was calculated 0.26 V vs Ag/AgCl **(Figure S14a).** We also tried to acquire CV measurements for H-Pz with ferrocene as an internal standard but in our observation, H-Pz compound was unstable with ferrocene **(Figure S14b).** Thus, we couldn't test all materials with the inclusion of ferrocene under our testing conditions.

$$E_{HOMO}(\text{eV}) = E_{oxid} - E_{\frac{FC^+}{FC}} + 4.8 \quad \text{(v)}$$

$$E_{LUMO}(\text{eV}) = E_{HOMO}(\text{eV}) - E_{o-o}(\text{eV}) \quad \text{(vi)}$$

Computational studies were performed on the LUMS HPC facility using Gaussian 16; GaussView 6.0 was used to prepare input files and visualize results. Density of states (DOS) plots, DOS fragment contributions, and computed UV-Vis data were processed with GaussSum 2.2. Transition density matrices (TDM), charge density differences surface contours (CDD), transition density matrices heat maps and intramolecular charge-transfer and excitation contribution analyses were carried out using Multiwfn 3.8. Exciton binding energies (E_b) and reorganization energies for holes and electrons (λ_h, λ_e) were calculated using the respective equations (vii-x).

$$LHE = 1 - 10^{-f} \quad \text{(vii)}$$

$$E_b = \Delta E - E_x \quad \text{(viii)}$$

$$\lambda_h = \left[E_+^0 - E_0\right] + \left[E_0^+ - E_+\right] \quad \text{(ix)}$$

$$\lambda_e = \left[E_-^0 - E_0\right] + \left[E_0^- - E_-\right] \quad \text{(x)}$$

View Article Online
DOI: 10.1039/D6MA00215C

Here,
$\mathbf{E_0}$ = Ground state energy of molecule
$\mathbf{E_+}$ and $\mathbf{E_-}$ = Ground state energy of cations and anions
$\mathbf{E_+^0}$ and $\mathbf{E_-^0}$ = Neutral energies of cations and anions at ground state.
$\mathbf{E_0^+}$ and $\mathbf{E_0^-}$ = Cationic and anionic energies of optimized molecules at ground state.

Frontier molecular orbital distributions were visualized with Avogadro software. OriginPro 16 (Learning Edition) was used for graphs plotting, linear fitting and visualization.

Chemistry

Synthesis of 4-(4,4,5,5-tetramethyl-1,3,2-dioxaborolan-2-yl)-2,6-bis(trifluoromethyl) pyridine (A)

First, a Schlenk flask equipped with an oven dried magnetic stir bar was nitrogen purged followed by evacuated for three cycles. Next, $[Ir(OMe)(COD)]_2$ precatalyst (9.9 mg, 0.015 mmol, 1.5 mol %), 2,2'-bipyridine ligand (4 mg, 0.025 mmol, 2.5 mol %), pinacolborane (HBPin) (192 mg, 218 µL, 1.5 mmol, 1.5 equiv), and 2,6-bis(trifluoromethyl)pyridine substrate (215 mg, 1 mmol, 1 equiv) were added in the Schlenk flask respectively. Then, the Schlenk flask was closed, and the reaction mixture (RM) was heated at 80 °C using an oil bath for 3 h. The reaction progress was monitored by TLC and GC-MS analyses. Upon completion of reaction, the flask was brought out from oil bath, cooled at room temp., and the RM was exposed to air. The RM was concentrated under vacuum using rotary evaporator to remove volatiles. The crude RM was then purified by column chromatography using silica gel as stationary phase, hexane and DCM as eluents.
Compound A was isolated as a white solid (465 mg, 89 %); (Hexanes/DCM 1:3, R_f 0.41), mp 86-88 °C, GC-MS (EI), RT: 7.28, m/z (% relative intensity) 341.13 (M^+, 5), 326 (100), 322 (15), 299 (14), 281 (9), 255 (11).
Melting point, NMR and GC-MS data was in agreement with previously reported data in literature.[25]

General Procedure for Suzuki Coupling Reactions (H-Y):

All reactions of this study were carried out in oven dried Schlenk flask having a magnetic stir bar. First, Schlenk flask was nitrogen purged followed by evacuated for three cycles. Under positive supply of N_2, pre-catalyst $Pd(OAc)_2$ (9 mg, 0.04 mmol, 4 mol %), ligand SPhos (32.8 mg, 0.08 mmol, 8 mol %), 4-(4,4,5,5-tetramethyl-1,3,2-dioxaborolan-2-yl)-2,6-bis(trifluoromethyl)pyridine (853 mg, 2.5 mmol, 2.5 equiv) for entries (H-Pz to H-Per), limiting substrates [(1 mmol each, 1 equiv), base K_2CO_3 (414.6 mg, 0.03 mmol, 3 equiv) and 4 mL of toluene solvent were added in aforesaid order. After this, Schlenk flask was closed tightly and placed in an oil bath maintained at 80 °C for 8-24 h. The reaction progress was monitored by TLC and GC-MS analyses by taking crude mixture under N_2 atmosphere. Upon completion of reaction, flask was brought out from oil bath, cooled to room temp., and exposed to air. Next, mixture inside flask was extracted with DCM and EtOAc (20-30 mL x 3) and concentrated under vacuum using rotary evaporator to remove volatiles. The obtained crude mixture was then purified by column chromatography using silica gel as stationary phase, hexanes and DCM as eluents.

View Article Online
DOI: 10.1039/D6MA00215C

Synthesis of 2,5-bis(2,6-bis(trifluoromethyl)pyridin-4-yl)pyrazine (H-Pz)

General procedure was applied to 2,5-dibromopyrazine (238 mg, 1 mmol, 1 equiv) for 8 h, H-Pz compound was isolated as light-yellow solid (465 mg, 92 %); (Hexanes, R_f 0.74), mp 214-216 °C, ^{1}H NMR (400 MHz, $CDCl_3$) δ 9.39 (s, 2H), 8.61 (s, 4H);^{13}C NMR (151 MHz, $CDCl_3$) δ 150.4 (q, $^2J_{C–F}$ = 37.7 Hz, C), 148.6, 146.6, 142.3, 120.9 (q, $^1J_{C–F}$ = 276.3 Hz, CF_3),120.6; ^{19}F NMR (565 MHz, $CDCl_3$) δ -68.02 (s, CF_3); GC-MS (EI), RT: 11.77, m/z (% relative intensity) 506 (M^+, 51), 486 (26), 437 (5), 253 (9), 239 (90) 170 (100), 150 (18) 143 (12); FT-IR (neat) $\bar{\upsilon}$ (cm^{-1}) = 1613, 1389, 1326, 1286, 1264, 1190, 1129, 1101, 1019, 940, 919, 899, 856, 818, 719, 694, 658.

Synthesis of 4,7-bis(2,6-bis(trifluoromethyl)pyridin-4-yl)benzo[c][1,2,5]thiadiazole (H-BTD)

General procedure was applied to 4,7-dibromobenzo[c][1,2,5]thiadiazole (294 mg, 1 mmol, 1 equiv) for 19 h, H-BTD compound was isolated as red solid (400 mg, 71 %); (Hexanes/DCM 3:1, R_f 0.82), mp 202-204 °C, ^{1}H NMR (400 MHz, $CDCl_3$) δ 8.58 (s, 4H), 8.12 (s, 2H); ^{13}C NMR (151 MHz, $CDCl_3$) δ 153.3, 149.9, (q, $^2J_{C–F}$ = 36.2 Hz, C) 147.9, 131.1, 129.4, 123.3, 121.2 (q, $^1J_{C–F}$ = 274.8 Hz, CF_3); ^{19}F NMR (565 MHz, $CDCl_3$) δ -67.90 (s, CF_3); GC-MS (EI), RT: 13.89, m/z (% relative intensity) 562 (M^+, 100), 493 (36), 473 (26), 403 (7), 202 (9); FT-IR (neat) $\bar{\upsilon}$ (cm^{-1}) = 3095, 2922, 2850, 2015, 1608, 1394, 1333, 1281, 1200, 1129, 976, 905, 854, 803, 721, 701.

Synthesis of 6,12-bis(2,6-bis(trifluoromethyl)pyridin-4-yl)chrysene (H-Ch)

General procedure was applied to 6,12-dibromochrysene (386.1 mg, 1 mmol, 1 equiv) for 24 h, H-Ch compound was isolated as yellow solid (402 mg, 61 %); (Hexanes/DCM 3:1, R_f 0.7), mp 304-306 °C, ^{1}H NMR (400 MHz, $CDCl_3$) δ 8.90 (d, J = 8.5 Hz, 2H), 8.70 (s, 2H), 8.19 (s, 4H), 7.85 (dd, J = 15.4, 7.8 Hz, 4H), 7.74 (t, J = 7.6 Hz, 2H); ^{13}C NMR (151 MHz, $CDCl_3$) δ 153.4, 149.7 (q, $^2J_{C–F}$ = 36.2 Hz, C), 135.8, 131.2, 129.8, 128.5, 128.5, 128.4, 125.9, 124.8, 123.4 (q, $^1J_{C–F}$ = 274.8 Hz, CF_3), 120.4, 118.6; ^{19}F NMR (565 MHz, $CDCl_3$) δ -67.70 (s, CF_3); GC-MS (EI), RT: 20.45, m/z (% relative intensity) 654 (M^+, 100), 564 (8), 371 (15), 297 (17), 238 (19), 174 (10); FT-IR (neat) $\bar{\upsilon}$ (cm^{-1}) = 3080, 2931, 1603, 1520, 1440,1382, 1280, 1179, 1131, 1094, 987, 916, 884, 854, 763, 695.

Synthesis of 9,10-bis(2,6-bis(trifluoromethyl)pyridin-4-yl)anthracene (H-An)

General procedure was applied to 9,10-dibromoanthracene (336 mg, 1 mmol, 1 equiv) for 20 h, H-An compound was isolated as colourless solid (506 mg, 84 %); (Hexanes/DCM 3:1, R_f 0.72), mp 312-314 °C, GC-MS (EI), RT: 13.57, m/z (% relative intensity) 604 (M^+, 100), 535 (11), 465 (15), 370 (44), 300 (29), 251(33) 223 (11); FT-IR (neat) $\bar{\upsilon}$ (cm^{-1}) = 3045, 2921, 1607, 1426, 1339, 1279, 1188, 1133, 1029, 984, 916, 856, 806, 762,726, 698, 665, 647.
The mp, NMR and GC-MS data of this compound is in agreement with the literarture.[25]

Synthesis of 1,6-bis(2,6-bis(trifluoromethyl)pyridin-4-yl)pyrene (H-Py)

General procedure was applied to 1,6-dibromopyrene (360.1 mg, 1 mmol, 1 equiv) for 24 h, H-Py compound was isolated as light green solid (481 mg, 76 %); (Hexanes, R_f 0.37), mp 324-326 °C, ^{1}H NMR (400 MHz, $CDCl_3$) δ 8.38 (d, J = 7.9 Hz, 2H), 8.24 (d, J = 9.2 Hz, 2H), 8.18 (s, 4H), 8.07 (dd, J = 12.8, 8.6 Hz, 4H); ^{13}C NMR (101 MHz, Acetone-d_6) δ 154.6, 149.3 (q, $^2J_{C–F}$ = 36 Hz, C), 134.0, 132.9, 130.0, 129.4, 129.2, 126.8, 125.9, 125.5, 122.3 (q, $^1J_{C–F}$ =

View Article Online
DOI: 10.1039/D6MA00215C

274 Hz, CF_3); ^{19}F NMR (377 MHz, $CDCl_3$) δ -67.70 (s, CF_3); HRMS (ESI+): m/z $[M+H]^+$ calcd for $C_{30}H_{12}F_{13}N_2$ $[M+H]^+$: 629.0887; found: 629.0878; FT-IR (neat) $\bar{\upsilon}$ (cm^{-1}) = 3092, 2926, 2322, 2162, 1608, 1440, 1390, 1274, 1195, 1126, 1053, 994, 908, 844, 803, 723, 691.

Synthesis of 3,9-bis(2,6-bis(trifluoromethyl)pyridin-4-yl)perylene (H-Per)

General procedure was applied to 3,9-dibromoperylene (410.1 mg, 1 mmol, 1 equiv) for 24 h Following general procedure, H-Per compound was isolated as red solid (533 mg, 79 %); (Hexanes/DCM 5:1, R_f 0.52), mp 323-326 °C, ^1H NMR (400 MHz, $CDCl_3$) δ 8.38 (ddd, J = 7.8, 6.4, 3.9 Hz, 4H), 8.07 (s, 4H), 7.66 – 7.60 (m, 4H), 7.52 (d, J = 7.8 Hz, 2H), ^{13}C NMR (151 MHz, $CDCl_3$) δ 153.0, 149.6 (q, $^2J_{C-F}$ = 36.2 Hz, C), 135.4, 132.8, 132.1, 131.9, 129.3, 128.7 ((q, $^3J_{C-F}$ = 10.6 Hz, C), 125.3, 124.9, 124.5,122.2, 121.3(q, $^1J_{C-F}$ = 274.8 Hz, CF_3), 120.9; HRMS (ESI+): m/z $[M+H]^+$ calcd for $C_{34}H_{15}F_{12}N_2$: 679.1044; found: 679.1021; FT-IR (neat) $\bar{\upsilon}$ (cm^{-1}) = 3088, 2929, 2854, 2162, 1608, 1412, 1375, 1273, 1190, 1131, 933, 906, 882, 857, 830, 808, 724, 629.

Credit authorship contribution statement

Hasan Yaqoob: Investigation, Methodology, Data curation, Visualization, Formal analysis, Writing – original draft, conceptualization. **Nimra Arif:** Methodology, Formal analysis. **Rahman Shah Zaib Saleem:** Software, Formal analysis, Validation. **Jafar Iqbal Khan:** Formal analysis, Validation, Investigation. **Raja Shahid Ashraf:** Resources, Validation, Writing – review & editing. **Christian B. Nielsen:** Conceptualization, Resources, Validation, Supervision, Writing – review & editing. **Ghayoor Abbas Chotana**: Writing – review & editing, Supervision, Resources, Funding accusation, Project administration.

Conflicts of interest

The authors declare no competing financial or non-financial interests.

Acknowledgements

We are thankful to the Lahore University of Management Sciences (LUMS) for providing Lab infrastructure, Syed Babar Ali Foundation and LUMS Central Labs for analytical facilities. This research was funded by Higher Education Commission of Pakistan (HEC) grant number NRPU-5903 (to GAC), and by Lahore University of Management Sciences through Faculty initiative fund (FIF) grant number FIF-327 (to GAC). HY is thankful to HEC Pakistan for providing an IRSIP fellowship (57th batch - 72611) to join "The Nielsen Lab" as a visiting PhD student at Queen Mary University of London (QMUL), UK. We thank Dr. Stoichko Dimitrov (SPCS) and Dr. Flurin Eisner (SEMS), along with their PhD students Chun Hei Lau and Stanley Cazaly (QMUL), for providing access to the PL instrument facility and for their valuable assistance in acquiring the PL data. HY offers sincere gratitude to Dilara Gunturkun and Dr. Kalidass Kollimalaian for their assistance in electrochemical measurements.

References

1. Abid, Z.; Akram, W.; Marcial-Hernandez, R.; Gunturkun, D.; Shahid, M.; Altaf, M.; Min, J.; Khan, J. I.; Iqbal, J.; Rasul, S.; Nielsen, C. B.; Ashraf, R. S., Strategic Design,

Synthesis, and Computational Characterization of Hole Transport Materials for Lead-Free Perovskite Solar Cells. *ACS Sustainable Chemistry & Engineering* **2025,** *13* (2), 867-880.
2. Full, F.; Artigas, A.; Wiegand, K.; Volland, D.; Szkodzinska, K.; Coquerel, Y.; Nowak-Król, A., Controllable 1, 4-Palladium Aryl to Aryl Migration in Fused Systems─ Application to the Synthesis of Azaborole Multihelicenes. *Journal of the American Chemical Society* **2024,** *146* (42), 29245-29254.
3. Liu, W.; Shang, H.; Xu, X.; Bo, Z., Sustainable Organic Solar Cells: Materials Review, Molecular Design, and Device Engineering. *ACS Applied Engineering Materials* **2025,** *3* (5), 1102-1129.
4. Nielsen, C. B.; Ashraf, R. S.; Treat, N. D.; Schroeder, B. C.; Donaghey, J. E.; White, A. J.; Stingelin, N.; McCulloch, I., 2, 1, 3-Benzothiadiazole-5, 6-Dicarboxylic Imide–A Versatile Building Block for Additive-and Annealing-Free Processing of Organic Solar Cells with Efficiencies Exceeding 8%. *Advanced Materials* **2015,** *27* (5), 948-953.
5. Wang, Z.; Wang, H.; Tu, L.; Guo, Q.; He, W.; Shi, Y.; Zhou, E., A Dithienopyrazine-Based Wide Band Gap Polymer Donor for Efficient Organic Solar Cells. *ACS Applied Materials & Interfaces* **2025**.
6. Abid, Z.; Ali, L.; Shahid, M.; Nielsen, C. B.; Altaf, M.; Min, J.; Ashraf, R. S., Quantum modelling of multi-directional fused-ring electron acceptors for organic photovoltaics. *Journal of Physics and Chemistry of Solids* **2024,** *187*, 111837.
7. Rasool, F.; Wu, G.; Shafiq, I.; Kousar, S.; Abid, S.; Alhokbany, N.; Chen, K., Heterocyclic donor moiety effect on optical nonlinearity behavior of chrysene-based chromophores with push–pull configuration via the quantum chemical approach. *ACS omega* **2024,** *9* (3), 3596-3608.
8. Liu, J.; Zhu, W.; Zhou, K.; Wang, Z.; Zou, Y.; Meng, Q.; Li, J.; Zhen, Y.; Hu, W., Pyridyl-substituted anthracene derivatives with solid-state emission and charge transport properties. *Journal of Materials Chemistry C* **2016,** *4* (16), 3621-3627.
9. Kole, G. K.; Merz, J.; Amar, A.; Fontaine, B.; Boucekkine, A.; Nitsch, J.; Lorenzen, S.; Friedrich, A.; Krummenacher, I.; Košćak, M., 2-and 2, 7-Substituted para-N-Methylpyridinium Pyrenes: syntheses, molecular and electronic structures, photophysical, electrochemical, and spectroelectrochemical properties and binding to Double-Stranded (ds) DNA. *Chemistry–A European Journal* **2021,** *27* (8), 2837-2853.
10. Zhang, Y.; Shi, J.; Ji, L., B← N Lewis Pair-Functionalized Perylenes: Tuning Optoelectronic Properties via Regioisomerization. *The Journal of Organic Chemistry* **2025,** *90* (8), 3071-3077.
11. Geppert, P. T.; Volland, D.; Szkodzińska, K.; Nowak-Król, A., Synthetic Methods for the Construction of 1, 2-Azaborole-Containing Polycyclic Aromatic Hydrocarbons. *Organic Materials* **2025**.
12. Nowak-Król, A.; Geppert, P. T.; Naveen, K. R., Boron-containing helicenes as new generation of chiral materials: opportunities and challenges of leaving the flatland. *Chemical Science* **2024,** *15* (20), 7408-7440.
13. Pokladko-Kowar, M.; Gondek, E.; Danel, A.; Uchacz, T.; Szlachcic, P.; Wojtasik, K.; Karasiński, P., Trifluoromethyl substituted derivatives of pyrazoles as materials for photovoltaic and electroluminescent applications. *Crystals* **2022,** *12* (3), 434.
14. Wang, X.; Kong, W.; Jiang, T.; Xie, Z.; Zhang, J.; Ma, L.; Redshaw, C.; Zhao, Z.; Feng, X., Pyrene-Based Light-Harvesting Antenna Molecules. *The Journal of Physical Chemistry Letters* **2025,** *16* (10), 2468-2478.
15. Lu, Q.; Kole, G. K.; Friedrich, A.; Müller-Buschbaum, K.; Liu, Z.; Yu, X.; Marder, T. B., Comparison study of the site-effect on regioisomeric pyridyl–pyrene conjugates: synthesis, structures, and photophysical properties. *The Journal of Organic Chemistry* **2020,** *85* (6), 4256-4266.

View Article Online
DOI: 10.1039/D6MA00215C

16. Owada, T.; Sasabe, H.; Sukegawa, Y.; Watanabe, T.; Maruyama, T.; Watanabe, Y. Yokoyama, D.; Kido, J., A terpyridine-modified chrysene derivative as an electron transporter to improve the lifetime in phosphorescent OLEDs. *Journal of Materials Chemistry C* **2020,** *8* (9), 3200-3205.
17. Qin, G.; Lin, P.; Sun, X.; Guo, J.; Fan, J.; Ji, L.; Li, H.; Ren, A., Theoretically seeking charge transport materials with inherent mobility higher than 2, 6-diphenyl anthracene: three isomers of 2, 6-dipyridyl anthracene. *Physical Chemistry Chemical Physics* **2023,** *25* (1), 540-554.
18. Ragni, R.; Punzi, A.; Babudri, F.; Farinola, G. M., Organic and organometallic fluorinated materials for electronics and optoelectronics: A survey on recent research. *European Journal of Organic Chemistry* **2018,** *2018* (27-28), 3500-3519.
19. Mishra, D. R.; Sahoo, D. K.; Mishra, N. P., Recent Advances in Synthesis and Photophysical Applications of Pyridine-Based Heterocycles. *Asian Journal of Organic Chemistry* **2025,** *14* (6), e202500004.
20. Lv, M.; Wang, Q.; Zhang, J.; Wang, Y.; Zhang, Z. G.; Wang, T.; Zhang, H.; Lu, K.; Wei, Z.; Deng, D., Strengthening the hetero-molecular interactions in giant dimeric acceptors enables efficient organic solar cells. *Advanced Materials* **2024,** *36* (4), 2310046.
21. Dong, J.; Li, Y.; Liao, C.; Xu, X.; Yu, L.; Li, R.; Peng, Q., Dielectric constant engineering of nonfullerene acceptors enables a record fill factor of 83.58% and a high efficiency of 20.80% in organic solar cells. *Energy & Environmental Science* **2025,** *18* (10), 4982-4995.
22. El-Assaad, T. H.; Auer, M.; Castañeda, R.; Hallal, K. M.; Jradi, F. M.; Mosca, L.; Khnayzer, R. S.; Patra, D.; Timofeeva, T. V.; Brédas, J.-L., Tetraaryl pyrenes: photophysical properties, computational studies, crystal structures, and application in OLEDs. *Journal of Materials Chemistry C* **2016,** *4* (14), 3041-3058.
23. Baek, J.-Y.; Cheon, Y. R.; Shin, H.-g.; Park, J.-W.; Kim, Y.-H., New asymmetrical limb structured blue emitting material for OLED. *Optical Materials Express* **2014,** *4* (6), 1151-1158.
24. Idris, I.; Tannoux, T.; Derridj, F.; Dorcet, V.; Boixel, J.; Guerchais, V.; Soulé, J.-F.; Doucet, H., Effective modulation of the photoluminescence properties of 2, 1, 3-benzothiadiazoles and 2, 1, 3-benzoselenadiazoles by Pd-catalyzed C–H bond arylations. *Journal of Materials Chemistry C* **2018,** *6* (7), 1731-1737.
25. Batool, F.; Emwas, A.-H.; Gao, X.; Munawar, M. A.; Chotana, G. A., Synthesis and Suzuki Cross-Coupling Reactions of 2, 6-Bis (trifluoromethyl) pyridine-4-boronic Acid Pinacol Ester. *Synthesis* **2017,** *49* (06), 1327-1334.
26. Shahzadi, H. T.; Fatima, S.; Akhter, N.; Alazmi, M.; Nawaf, A.; Said, K. B.; AlGhadhban, A.; Sulieman, A. M. E.; Saleem, R. S. Z.; Chotana, G. A., Iridium-Catalyzed C–H Borylation of CF3-Substituted Pyridines. *ACS omega* **2022,** *7* (13), 11460-11472.
27. Chizhov, D. L.; Kvashnin, Y. A.; Demina, N. S.; Zhilina, E. F.; Minin, A. S.; Verbitskaia, N. A.; Dinastiia, E. M.; Rusinov, G. L.; Verbitskiy, E. V.; Charushin, V. N., Novel CF_3-Substituted Pyridine-and Pyrimidine-Based Fluorescent Probes for Lipid Droplet Bioimaging. *International Journal of Molecular Sciences* **2025,** *26* (11), 5271.
28. Yamaji, M.; Yoshikawa, I.; Mutai, T.; Houjou, H.; Goto, K.; Tani, F.; Suzuki, K.; Okamoto, H., Elucidation of the relationship between solid-state photoluminescence and crystal structures in 2, 6-substituted naphthalene derivatives. *Journal of the Chinese Chemical Society* **2025,** *72* (10), 1145-1152.
29. Haubitz, T.; Fudickar, W.; Linker, T.; Kumke, M. U., pH-Sensitive Fluorescence Switching of Pyridylanthracenes: The Effect of the Isomeric Pattern. *The Journal of Physical Chemistry A* **2020,** *124* (52), 11017-11024.

30. Chaiwai, C.; Kitisriworaphan, W.; Petdee, S.; Chawanpunyawat, T.; Chasing, P.; Nalaoh, P.; Manyum, T.; Sudyodsuk, T.; Promarak, V., Red-Emitting Fluorophores Featuring Combined Hybridized Local and Charge-Transfer Excited State and Aggregation-Induced Emission as Efficient Emitters for Electroluminescent Devices. *ChemPhotoChem* **2023,** *7* (7), e202300022.
31. Woldegiorges, K.; Belay, A.; Kebede, A.; Abebe, T., Estimating the ground and excited state dipole moments of levofloxacin and norfloxacin drugs using solvatochromic effects and computational work. *Journal of Spectroscopy* **2021,** *2021* (1), 7214182.
32. Patil, S. A.; Kadolkar, P. S.; Wari, M. N.; Inamdar, S. R., Photo-physical study of coumarins in aqueous organic solvents: an experimental and theoretical approach. *Materials Today Communications* **2021,** *29*, 102733.
33. Fatma, N.; Mehata, M. S.; Pandey, N.; Pant, S., Experimental and theoretical interpretations of spectral behavior of 6-methoxyflavone. *Journal of Photochemistry and Photobiology A: Chemistry* **2021,** *404*, 112945.
34. Kumar, D.; Thomas, K. J., Optical properties of pyrene and anthracene containing imidazoles: experimental and theoretical investigations. *Journal of Photochemistry and Photobiology A: Chemistry* **2011,** *218* (1), 162-173.
35. Ahn, M.; Kim, M.-J.; Wee, K.-R., Electron push–pull effects in 3, 9-bis (p-(R)-diphenylamino) perylene and constraint on emission color tuning. *The Journal of Organic Chemistry* **2019,** *84* (18), 12050-12057.
36. Guesmi, N. E., Solvent effect on the photophysical properties of terpyridine incorporating pyrene moiety: Estimation of dipole moments by solvatochromic shift Methods. *Journal of Fluorescence* **2023,** *33* (6), 2315-2326.
37. Debata, B. P.; Dash, J.; Patel, S.; Vaidyanathan, S., HLCT-AIE active deep blue fluorophores and their versatile applications: a multifunctional approach for advanced white LED materials, picric acid sensing and fingerprint visualization. *Journal of Materials Chemistry C* **2025**.
38. Aydemir, M.; Haykir, G.; Demir, S.; Aydemir, E.; Arslan, E.; Selvitopi, H.; Arslan, M. E.; Kadı, A.; Monkman, A. P.; Turksoy, F., Anthracene–pyridine derivatives as fluorescent probes: The role of nitrogen positioning in bioimaging performance. *Journal of Photochemistry and Photobiology A: Chemistry* **2025**, 116666.
39. Han, X.; Gong, W.; Tong, Y.; Wei, D.; Wang, Y.; Ding, J.; Hou, H.; Song, Y., Synthesis and properties of benzothiadiazole-pyridine system: The modulation of optical feature. *Dyes and Pigments* **2017,** *137*, 135-142.
40. Neto, B. A.; Carvalho, P. H.; Santos, D. C.; Gatto, C. C.; Ramos, L. M.; de Vasconcelos, N. M.; Corrêa, J. R.; Costa, M. B.; de Oliveira, H. C.; Silva, R. G., Synthesis, properties and highly selective mitochondria staining with novel, stable and superior benzothiadiazole fluorescent probes. *Rsc Advances* **2012,** *2* (4), 1524-1532.
41. Omer, K. M.; Ku, S.-Y.; Wong, K.-T.; Bard, A. J., Green electrogenerated chemiluminescence of highly fluorescent benzothiadiazole and fluorene derivatives. *Journal of the American Chemical Society* **2009,** *131* (30), 10733-10741.
42. Hou, J.; Cheng, Y.; Yan, T.; Liu, Z.; Kang, P., High-efficiency electrochemical air capture enabled by thiadiazole redox carrier with tunable gas-selective channels. *Nature Communications* **2026**.
43. Konkol, K. L.; Wilcox, W. D.; Rasmussen, S. C., 2, 3-Bis (2-pyridyl) thieno [3, 4-b] pyrazine and its ruthenium (II) complexes: a new bidentate bridging ligand for enhanced metal–metal communication. *Dalton Transactions* **2024,** *53* (40), 16685-16692.
44. Ward, J. S.; Danos, A.; Stachelek, P.; Fox, M. A.; Batsanov, A. S.; Monkman, A. P.; Bryce, M. R., Exploiting trifluoromethyl substituents for tuning orbital character of singlet

and triplet states to increase the rate of thermally activated delayed fluorescence. *Materials Chemistry Frontiers* **2020,** *4* (12), 3602-3615.
45. Jiang, W.; Li, Y.; Yue, W.; Zhen, Y.; Qu, J.; Wang, Z., One-pot facile synthesis of pyridyl annelated perylene bisimides. *Organic Letters* **2010,** *12* (2), 228-231.
46. Yin, Y.; Shi, R.; Liu, Z.; Li, Y.; Jiang, T.; Zhao, L.; Li, J.; Ji, D.; Li, L.; Fei, Z., Design, synthesis, and optoelectronic properties of benzothiadiazole-fused sulfur and nitrogen-containing polycyclic heteroaromatics. *Journal of Materials Chemistry C* **2025,** *13* (3), 1281-1291.
47. Jia, J.; Zhang, T.; Lu, Y.; Wu, X.; Song, Y., Dramatically enhanced broadband reverse saturable absorption of anthracene derivatives: Regulatory effect of π-bridge in two-branched molecules. *Journal of Photochemistry and Photobiology A: Chemistry* **2025**, 116768.
48. Dong, G.; Luo, H.; Chen, F.; Peng, Z.; Xu, C.; Wang, J.; Gao, S.; Zhang, J.; Yang, Y., Study on Mechanofluorochromism and Ink-Free Writing of Two Anthracene-Substituted Pyridine-Based Difluoroboron Compounds. *ChemistrySelect* **2025,** *10* (25), e00469.
49. Montanaro, S.; Gillett, A. J.; Kimber, P.; Xing, D.; Feldmann, S.; Evans, E. W.; Warrington, S.; Plasser, F.; Friend, R. H.; Wright, I. A., Elucidating the non-radiative losses encountered in intramolecular charge transfer compounds with benzodithiophene-4, 8-dione acceptors. *Journal of Materials Chemistry C* **2024,** *12* (35), 14021-14030.
50. Javed, M.; Akram, W.; Ali, Z.; Shahzad, N.; Shahid, M.; Chotana, G. A.; Khan, J. I.; Min, J.; Altaf, M.; Nielsen, C. B., Molecular engineering, synthesis, and atomistic structure–property relationship of indoloquinoxaline-capped small donors for efficient organic solar cells. *Journal of Materials Chemistry C* **2025,** *13* (42), 21528-21543.
51. Yaqoob, H.; Nawaz, M.; Saleem, R. S. Z.; Chotana, G. A., Synthesis, Characterization, Photophysical, Electrochemical, and DFT Studies of Perylene-Based D-π-A-π-D Molecules for Optoelectronic Applications. *Journal of Photochemistry and Photobiology A: Chemistry* **2026,** *470*, 116661.
52. Weissenseel, S.; Drigo, N. A.; Kudriashova, L. G.; Schmid, M.; Morgenstern, T.; Lin, K.-H.; Prlj, A.; Corminboeuf, C.; Sperlich, A.; Brütting, W., Getting the right twist: influence of donor–acceptor dihedral angle on exciton kinetics and singlet–triplet gap in deep blue thermally activated delayed fluorescence emitter. *The Journal of Physical Chemistry C* **2019,** *123* (45), 27778-27784.
53. Akram, W.; Walayat, A.; Zahid, W. A.; Khan, G. S.; Alanazi, M. M.; Elmushyakhi, A.; Iqbal, J., Rational Design and Engineering of Terminal Functional Groups in Dibenzothiophene-Diphenylamine Small Molecular Electron Donors for Enhanced Photovoltaic Efficiency in All-Small-Molecule Organic Solar Cells. *Advanced Theory and Simulations* **2024,** *7* (8), 2400289.
54. Akram, W.; Walayat, A.; Zahid, W. A.; Peng, T.; El Maati, L. A.; Alomar, M.; Tawfik, S. G.; Iqbal, J., Molecularly engineered pyrrole-based hole transport materials featuring diversified structures for high-performance perovskite solar cells from first-principles. *Journal of Molecular Liquids* **2024,** *405*, 125103.
55. Mester, D.; Kállay, M., Charge-transfer excitations within density functional theory: How accurate are the most recommended approaches? *Journal of Chemical Theory and Computation* **2022,** *18* (3), 1646-1662.
56. Akram, W.; Zahid, W. A.; El Maati, L. A.; Altuijri, R.; Hossain, I.; Akhter, M. S.; Iqbal, J., Engineering push–pull structural versatility in highly functional carbazole-based hole transporting materials design for efficient perovskites solar devices. *Journal of Photochemistry and Photobiology A: Chemistry* **2023,** *444*, 114991.

View Article Online
DOI: 10.1039/D6MA00215C

The spectroscopic data (^{1}H and ^{13}C NMR, and mass spectra) supporting this article have been uploaded as part of the electronic supplementary information (ESI)